ChemistrySelect

ChemistrySelect
Chemistry Europe
European Chemical Societies Publishing

RESEARCH ARTICLE

Hafnium-Modified LATP NASICON Ceramics as High-Performance Solid Electrolytes for Lithium-Ion Batteries

A. Panneerselvam[1] | R. Senthil kumar[2] | V. M. Senthilkumar[3] | Kallapalli Anjani Devi[4] | S. Selvakumar[5] | S. C. Vella Durai[6]

[1]Department of Physics, Vivekanandha College of Engineering for Women (Autonomous), Namakkal, Tamil Nadu, India | [2]Department of Physics, T.J.S. Engineering College, Peruvoyal, Tamil Nadu, India | [3]Department of Electronics Engineering (VLSI Design and Technology), Rajalakshmi Institute of Technology, Chennai, Tamil Nadu, India | [4]Department of Physics, Aditya University, Surampalem, Andhra Pradesh, India | [5]Department of Science and Humanities, Thamirabharani Engineering College (Autonomous), Tirunelveli, Tamil Nadu, India | [6]PG and Research Department of Physics, Sri Paramakalyani College, Tenkasi, Tamil Nadu, India

Correspondence: A. Panneerselvam (panneer.phy@gmail.com)

Received: 11 April 2026 | **Revised:** 26 August 2026 | **Accepted:** 3 September 2026

Keywords: aliovalent dopant | NASICON | ceramic electrolyte | structural stability | ionic transport

ABSTRACT

Solid-state lithium-ion batteries (SSLIBs) are emerging as a promising next-generation energy storage technology because they replace flammable liquid electrolytes with solid ones, improving safety and thermal stability. Among available materials, NASICON-type LATP has received considerable attention due to its high lithium-ion conductivity at room temperature and strong structural stability. It is well established that cation doping can enhance lithium-ion transport, suppress titanium reduction, and stabilize the LATP framework. In this study, aliovalent tetravalent hafnium (Hf^{4+}) doping in the LATP NASICON structure, along with aluminum, is systematically investigated to improve structural stability and ionic conductivity. Hf^{4+}-doped LATP ceramics were synthesized using a solid-state reaction method, and the effects of doping on crystal structure, microstructure, and conductivity were examined. Structural analysis confirms that Hf^{4+} is successfully incorporated into the LATP lattice without forming secondary phases, while morphological studies indicate improved grain connectivity and densification. Electrochemical impedance spectroscopy shows a clear enhancement in lithium-ion conductivity for Hf^{4+}-doped LATP compared to undoped and lower-valence doped samples. This improvement is attributed to better lattice stability, reduced Ti^{4+} reduction, and more efficient lithium-ion migration pathways. These results demonstrate that Hf^{4+} doping is more effective than divalent or trivalent doping strategies.

1 | Introduction

Lithium-ion batteries (LIBs) are more efficient, have a longer service life, and have a greater specific energy. With a yearly production capacity of roughly one billion cells, these characteristics have made LIBs the most favored power source for the consumer electronics sector. Because of their drawbacks, which include potential leakage, flammability, electrochemical instability, and so forth, current commercial LIBs that use liquid electrolytes do not fully ensure the safety of an electronic device. By halting breakdown processes, the inclusion of a solid electrolyte increases LIB safety and extends their service life [1–4]. Solid-state inorganic batteries offer significant benefits over conventional liquid electrolyte systems in terms of safety, operating temperature range, and electrochemical stability window. Based on inorganic amorphous or ceramic solid electrolytes

All rights reserved, including rights for text and data mining and training of artificial intelligence technologies or similar technologies.
© 2026 Wiley-VCH GmbH

(SE), fully inorganic solid-state batteries are incredibly stable and devoid of combustible materials. SE with a NASICON-type structure has a high Li-ion room-temperature conductivity in the 10^{-6}–10^{-3} S cm^{-1} range, is stable in water and air, and has the lowest activation energy for Li-ion conduction. Trigonal crystal symmetry is typically observed in the NASICON-type electrolytes, which have the general formula $NaM_2(PO_4)_3$. The presence of a system of cavities that create a 3D network of channels that allow alkali ions to move through is what makes the structure unique. SE characteristics can be altered by small structural modifications, such as heterovalent doping. $LiTi_2(PO_4)_3$ (LTP) was identified as a material with good chemical and thermal stability and a total ionic conductivity of 10^{-6} S cm^{-1} among a wide range of SE NASICONs [5–8]. The conductivity was raised to 10^{-3} S cm^{-1} by heterovalently substituting Al cation (0.3 Al per formula unit) into the Ti site. The final compound had the general formula $Li_{1+x}Al_xTi_{2-x}(PO_4)_3$ (LATP) and maintained the NASICON structural type. However, Ti^{4+} reduction to Ti^{3+} causes LATP's surface to gradually deteriorate in contact with Li metal. This lowers ionic conductivity at the electrolyte–electrode interface, delaying or even stopping the migration of Li-ions. Metallic Li reduction has no effect on Hf, although molecules like $LiM_2(PO_4)_3$ (M = Hf) are structurally identical to LATP. Compared to Ti^{4+} (0.605 Å), Hf^{4+} has a larger ionic radius (0.71 Å). Changes in the average M^{4+} cation ionic radius were shown to affect the electrochemical properties of $LiM_2(PO_4)_3$ (M = Zr) [9–12]. Moreover, alkaline earth minerals are one type of doping element that is commonly employed since they have greater reserves than rare earth materials. For example, doping $Li_{1.5}Al_{0.5}Ge_{1.5}(PO_4)_3$ with Mg results in an increase in Li-ion concentration and an expansion of Li-ion conducting channels because Mg^{2+} (0.72 Å) has a larger ionic radius than Ge^{4+} (0.53 Å) and Al^{3+} (0.54 Å). $Li_{1.6}Al_{0.4}Mg_{0.1}Ge_{1.5}(PO_4)_3$ was found to have an ionic conductivity of 7.4×10^{-3} S cm^{-1}, which is higher than $Li_{1.5}Al_{0.5}Ge_{1.5}(PO_4)_3$ – 2.9×10^{-3} S cm^{-1}. In the LATP, Mg^{2+} can also partially substitute Al^{3+}. More Li-ions must be added to the crystal lattice to lower the total positive charge while maintaining electroneutrality [13–16]. Consequently, an increase in the number of charge carriers is thought to improve conductivity. Other divalent metals with comparable characteristics, like Ca^{2+} and Sr^{2+}, were substituted using comparable techniques. It is believed that the migration of Li-ions is facilitated by the increased size of Sr^{2+} relative to Al^{3+}, which permits the crystal lattice to expand. Compounds with a higher concentration of Li-ion carriers can be synthesized simultaneously based on the need of electro neutrality since the Sr^{2+} cation is smaller than the Al^{3+} cation. Therefore, when Sr^{2+} is partially substituted for Al^{3+} in LATP, an increase in ionic conductivity might be expected [17–19]. Even if NASICON doping using different techniques is a reasonably mature subject, research on doping substances and Al in LATP simultaneously is yet somewhat unexplored. Thus, investigating the potential for heterovalent partial cationic substitution in NASICONs containing Al is intriguing. This work's main objective is to create LATP by partially replacing Ti with tetra-(Hf) valents. The most popular synthesis technique, the solid-state reaction approach, in which the precursors are ground, was selected because to the synthesis difficulty related to precursor selection. Additionally, this work offers a thorough analysis of how doping affects both the inhibition of Ti^{4+} reduction at the interface with Li metal and the ionic conductivity of modified LATP.

2 | Experimental Section

2.1 | Materials Synthesis

The generic formula $Li_{1.3+y}Al_{0.3}M_xTi_{1.7-x}(PO_4)_3$, where M = Hf, was used to create the samples with a tetravalent cation substitution. LATP (M_x), where M is the doping cation and x is its quantity, is another way to represent the samples. Precursors supplied by Sigma–Aldrich included $LiNO_3$ (97%), Al_2O_3 (99%), TiO_2 (99.7%), and a doping agent from HfO_2 (98%), and $NH_4H_2PO_4$ (99%). To lessen the loss of Li during sintering, an extra 10% of surplus Li was supplied to each sample during the first stage of precursor preparation. First, water-soluble precursors ($LiNO_3$, $NH_4H_2PO_4$) were thoroughly mixed in deionized water until they completely dissolved. The solution was then supplemented with metal oxides and urea $(NH_2)_2CO$ (99.5%), which is twice the amount of loaded $NH_4H_2PO_4$. The water volume was 25 mL, and the total mass of the dry components was roughly 20 g. A magnetic stirrer was used to mix the produced solution at 70°C for 12 h until it dried. After that, the combination was annealed for 8 hours at 700°C in the air. After the final product was ground in an agate mortar, the crystalline powder was compressed under 10 tons of pressure (1.25 GPa) into pellets with a diameter of 10 mm. The pellets were also sintered in air for 6 hours at 900°C. The samples with the divalent cation substitution were also generated by a traditional solid-state method using the same chemicals, with an intermediate treatment at 500°C for 8 h and a subsequent sintering at 850°C for 6 h in air due to preparation challenges.

2.2 | Characterization

The crystal structures and phases in the generated samples were determined using a Bruker D8 Advance x-ray powder diffractometer with CuKα radiation (λ = 1.5418 Å). A TESCAN VEGA3 LMU scanning electron microscope (SEM) was used to analyze the microstructures and morphologies. A WITEC ALPHA 300-R Raman spectrometer, which operates with a 532 nm source wavelength in the frequency range of 0–1200 cm^{-1}, was used to gather the Raman spectra. The Li^+ conductivity was evaluated using both methods. Ion-blocking electrodes were created by depositing silver onto the solid electrolyte. Silver paste was applied to both sides of the pellet for conductivity measurements, and the Ag/pellet/Ag symmetric cells were subjected to electrochemical impedance spectroscopy (EIS) utilizing a VMP3 (Bio-logic) device. The AC amplitude was 500 mV, and the frequency range used was from 1 to 10 mHz. The pellets were allowed to attain equilibrium at target temperatures of 30°C and 120°C ± 1°C for at least 15 min before impedance testing. EIS measurements were performed throughout a variety of temperatures.

3 | Results and Discussion

3.1 | Structural Analysis

XRD analysis was conducted to ascertain whether the samples obtained exhibited the NASICON structure; the findings are depicted in Figure 1. A pure NASICON-type structure was

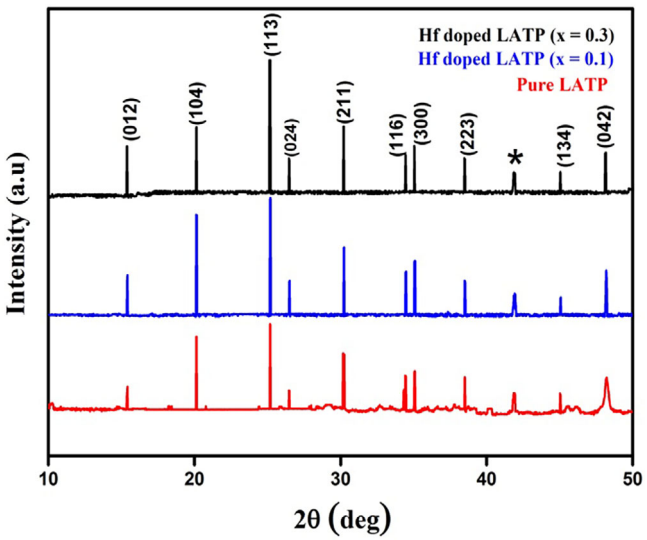


FIGURE 1 | Typical XRD patterns of pure and hafnium-doped LATP powders.

observed only when the atomic percentage of the dopants was below $x = 0.3$, where x denotes the atomic unit of the doping cation, among the other two selected concentrations of the tetravalent Hafnium cation dopant. An example pattern indicative of a NASICON structure featuring a trigonal space group of R3c is illustrated in the diffraction plots of all the synthesized materials in Figure 1. The absence of impurities in the XRD patterns with tetravalent cation doping (Hf^{4+}) suggests that the desired compositions were successfully synthesized. The peak splitting observed in the XRD pattern results from the crystallization of pure LATP into a monoclinic crystal system rather than a trigonal one, as was previously described [20–22]. Nevertheless, there was no splitting peak at the prescribed doping levels, indicating that there was no change in symmetry after the doping.

Additionally, adding dopants at higher concentrations ($x = 0.3$) caused a noticeable phase separation. A phase separation for these compositions is somewhat surprising because Al-free phases are currently known. This phenomenon may be explained by an instability brought on by a smaller Al^{3+} cation in the presence of bulky Hf^{4+}. The cell parameters for Hf-based systems should grow with increasing doping cation content. Given that the atomic radius and unit cell for Ti ($r_{Ti}{}^{4+} = 0.605$ Å) is smaller than that of Hf ($r_{Hf}{}^{4+} = 0.71$ Å), the addition of larger atoms usually causes the atomic radius and unit cell to extend. This suggests that the dopants were successfully integrated into the structure. Because Hf^{4+} have the same size, the cell characteristics of samples containing Hf with the same doping levels are highly similar. Such a significant shift would cause a discernible number of impurities in the XRD pattern if there is no doping. Lattice parameters of Hf-doped LATP electrolyte powders are summarized in Table 1.

3.2 | FTIR Analysis

Figure 2 illustrates how FTIR analysis was used to examine the bonds in Hf-doped LATP. The stretching vibrations of the P-O

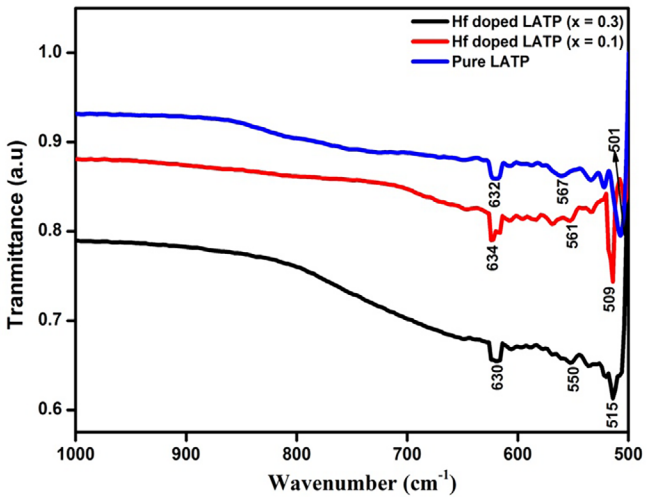


FIGURE 2 | FT-IR Spectra of Hf-doped LATP solid electrolytes.

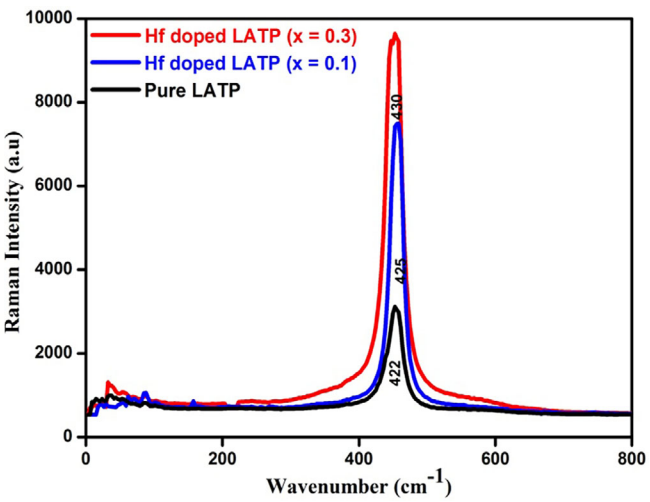


FIGURE 3 | Raman Spectra of Hf doped LATP solid electrolytes.

bond in the PO_4 tetrahedra [23] are responsible for the LATP bands at 630 and 550 cm^{-1}. The peak at 634 cm^{-1} is associated with the stretching of the P—O bond. Additionally, the LATP-doped Hafnium sample had a little peak at 542 cm^{-1}, which is linked to the Hf—O—Hf Silanol Bridge's symmetric stretching vibrations. Additionally, the peak in the 500–500 cm^{-1} range suggests the creation of Hf—O bonds. This suggests that Hafnium has been added to our substance. The concentration of intensity peaks between 600 and 650 cm^{-1} represents the Ti—O stretching vibrations of the TiO_6 octahedron. The O—H stretching vibrations caused by moisture contained in the material are associated with peaks in the range of 950–1000 cm^{-1} that are undetectable to the unaided eye.

3.3 | Raman Spectra

Figure 3 shows the Raman spectra of Hafnium-doped LATP samples at different concentrations. For $x = 0.00$, 0.1, and 0.3, respectively, there are notable symmetric stretching modes at 450, 461, and 461 cm^{-1}. The Raman spectroscopy investigation shown in Figure 3 provides a detailed understanding of the

TABLE 1 | Lattice parameters of Hf doped LATP electrolyte powders.

	a (Å)	c (Å)	V (Å^3)
Pure LATP	7.634	21.17	1203.16
Hf doped LATP $x = 0.1$	7.649	21.02	1230.40
Hf doped LATP $x = 0.3$	7.654	20.09	1210.01

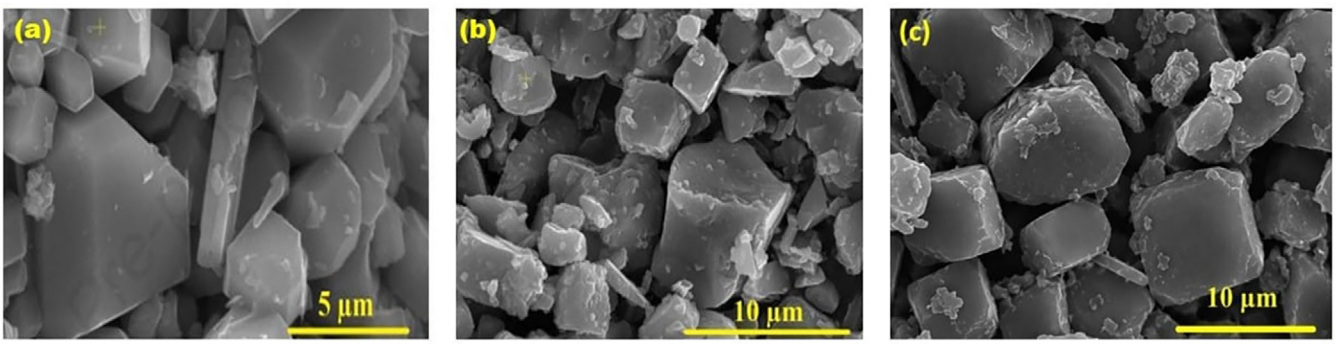


FIGURE 4 | SEM images of (a) LATP, (b) Hf-doped LATP, and (c) Hf-doped LATP after contact with Li. The scale bars are 5 µm for (a) and 10 µm for (b) and (c).

structural properties of LATP electrolyte samples, each of which has varying concentrations of Hf^{4+} ions. From 0 to 800 cm^{-1}, this data provides a comprehensive insight of these materials' vibrational behavior.

One key observation from the Raman spectra is the prominent Raman-active vibration peak at 422 cm^{-1} found in all samples. The symmetrical arrangement of oxygen ions around each Li^{3+} cation, which is a key feature of the NASICON structure, is represented by this peak, highlighting the F_2g vibration mode of the cubic lattice. As the concentration of Hf^{4+} ions increases, the amplitude of the F2g vibration notably rises, indicating the effect of Hf^{4+} doping. The increase in amplitude results from the Hf^{4+} ions generating additional lattice planes, which disrupt the original symmetry and weaken the F_2g mode. A little shift in the F_2g mode peak position with increasing Hf^{4+} concentration, indicating changes in the lattice properties and the immediate environment around the Ti^{4+} cations, provides more evidence that Hf^{4+} considerably influences the structural aspects of LATP electrolytes [24]. In summary, our work successfully illustrates how the addition of Hf^{4+} ions alters the lattice structure and vibrational properties of LATP electrolytes, offering vital insight into the impact of doping on these materials.

3.4 | Morphological Analysis

The morphology of the electrolytes was examined and compared with their initial morphology, as shown in Figure 4. Figure 4a,b presents the initial morphologies of the LATP and Hf-doped solid electrolytes, respectively. Both samples consist of faceted particles with well-defined crystal surfaces. The particle sizes are in the micrometre range, with some larger agglomerated particles also observed. These agglomerates may be related to the electrolyte synthesis process. Figure 4c shows the morphology of the electrolyte after contact with Li. The particles remain distributed, whereas the crystal facets become less distinct compared with those of the fresh samples shown in Figure 4a,b. These morphological changes may result from the interaction between the electrolyte and Li. The Hf-doped sample shows well-defined crystal facets, which may be associated with the incorporation of Hf^{4+} ions into the LATP structure [25].

TABLE 2 | Conductivity values of Pure LATP &Hf doped LATP electrolytes at room temperature.

Electrolytes	Room temperature (S cm^{-1})
Pure LATP	7.12×10^{-6}
Hf doped LATP ($x = 0.1$)	8.31×10^{-5}
Hf doped LATP ($x = 0.3$)	4.03×10^{-4}

3.5 | Electrochemical Characterization

An EIS analysis was conducted to assess the ionic conductivity of the doped samples, and the results are presented in Figure 5 (with fitted data). The summarized values for ionic conductivity for ion migration are listed in Table 2. Given that the conductivity measurements are influenced by numerous factors, an initial undoped LATP served as a reference point. The undoped sample exhibited a conductivity of 7.12×10^{-6} S cm^{-1}, with a pellet density of 91% of the theoretical, which is an order of magnitude lower than what is typically reported in the literature.

From Table 2, it is notable that doping with both lower & higher concentrations of cations does not significantly alter the conductivity of the material, indicating that the pathways for ion transport in the crystal lattice remain unchanged. A more pronounced and anticipated correlation is seen with the

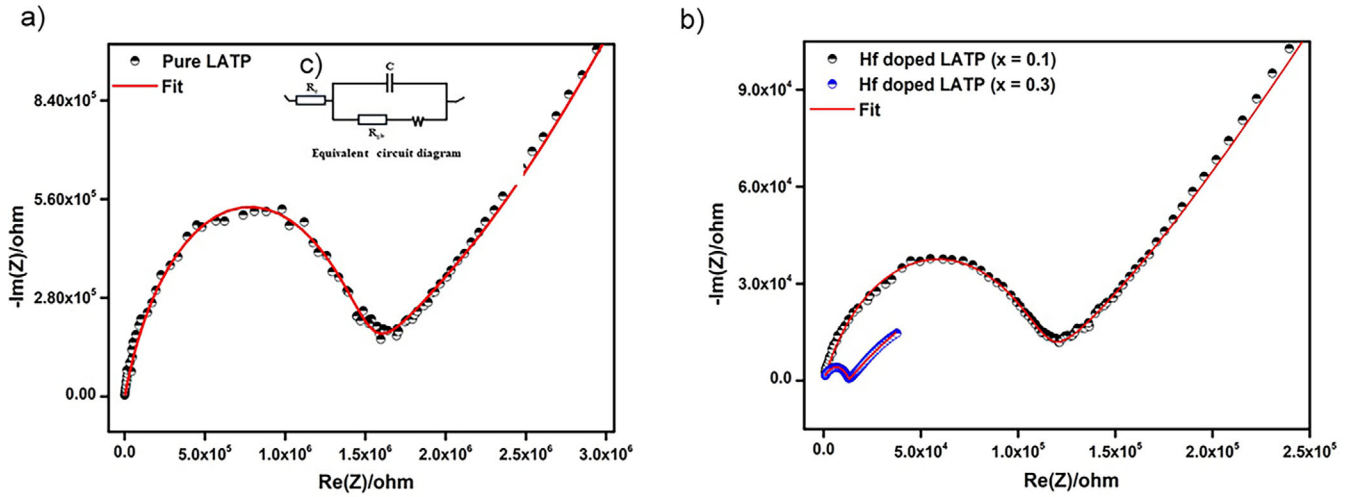


FIGURE 5 | Nyquist plots of Hf-doped LATP electrolytes measured at room temperature for (a) $x = 0.0$, (b) $x = 0.1$, and $x = 0.3$.

density of the pellet: samples that are denser show greater conductivity.

Nevertheless, even with this observation in mind, it remains challenging to make definitive conclusions about the significant differences among samples due to the constraints of EIS measurements, where numerous variables influence the overall conductivity. Thus, it appears that the partial substitution of the cations did not impact the system's conductivity. To assess the ionic conductivity of the series, electrochemical impedance spectra (EIS) for Hafnium-doped LATP were recorded, as illustrated in Figure 5. A semicircular feature is apparent in the impedance spectra at high frequencies, while at lower frequencies, a slanted line can be seen. This inclined line is indicative of the diffusion of lithium ions through the blocking gold electrodes. The semicircle's diameter signifies the resistance at the grain boundary, just as the left intercept at high frequencies denotes the bulk resistance. Consequently, the total impedance (R) found in this study includes both the bulk resistance (R_b) and the grain boundary resistance (R_{gb}), expressed as $R = R_b + R_{gb}$. Due to the limitations in frequency of the electrochemical workstation, the bulk resistance area remains unobservable. The resistance measurements for R_b and R_{gb} were conducted at ambient temperature, as illustrated in Table 2; the Nyquist plot was generated by fitting it to the pertinent circuit diagram shown in the inset of Figure 5. The figure displays the Nyquist plot, while the table lists the values obtained for R_b, R_{gb}, and the ionic conductivities of LATP with Hf-doping. The overall conductivity is mainly determined by lithium-ion movement across the grain boundary, which initially showed a decrease followed by an increase with the addition of Hafnium. The analysis revealed that the peak value of the measured parameter occurred at a doping concentration of 0.3; however, above this concentration, there was a reduction in ionic conductivity as the doping levels increased. The decrease can be explained by the accumulation of non-lithium ions, with excess Hafnium phases forming at the grain boundaries, which obstructs lithium-ion conduction. Moreover, the buildup of hafnium metal ions at the grain boundaries may contribute to binding the grains together, thereby increasing the compaction density of solid electrolytes. This phase might also promote the movement of Li^+ ions from the grain core to the boundary phases, improving the ionic conductivity along the grain boundaries. Electrochemical impedance spectroscopy indicates that pure LATP has the lowest impedance value of 7.12×10^{-6} S cm^{-1} and Hafnium doped LATP—$x = 0.3$ obtained a higher ionic conductivity of 4.03×10^{-4} S cm^{-1} at room temperature. From EIS perspective, the ionic conductivity increases at $x = 0.3$. What about other series of increasing and decreasing doping of Hf amount, like $x = 0.5$ or $x = 0.2$. At $x = 0.2$, the dopant concentration was relatively low, and therefore, the formation of oxygen vacancies was insufficient to significantly enhance the ionic conductivity. Consequently, the room-temperature ionic conductivity was relatively low. In contrast, at $x = 0.5$, the higher dopant concentration may lead to an excess of dopant ions, which can act as barriers or block the mobility of oxygen ions, resulting in higher resistance compared with the $x = 0.3$ composition. The $x = 0.3$ composition was found to provide an optimum dopant concentration, resulting in a favorable concentration of oxygen vacancies and enhanced ionic conductivity.

4 | Conclusion

The NASICON-type LATP ceramic solid electrolyte was modified with heterovalent dopants while maintaining the Al content through both the molten flux and solid-state technique. The effect of various dopants and their amounts on the ionic conductivity and the reduction of Ti^{4+} in the modified LATP solid electrolytes was thoroughly investigated. Our findings indicate that doping at low ratios does not considerably influence the conductivity, but alters its redox properties. Tetravalent cations of similar dimensions (Hf^{4+}) appear to inhibit the reduction of Ti^{4+}. This occurrence reveals a weakness of LATP when it comes to divalent cation impurities. The significance of this finding highlights the need to increase the standards for potential LATP manufacturing, where it is essential to carefully eliminate divalent cation impurities during the synthesis process to obtain a higher-quality product. Moreover, we discovered that the morphology and crystallinity of the LATP surface could significantly affect not only the diffusion system between the electrode and electrolyte but also the potential catalytic characteristics. The findings presented in this work offer crucial synthesis details and scientific

insights necessary for developing LATP-based solid electrolytes that exhibit high ionic conductivity and reduced sensitivity to Ti^{4+} reduction.

Author Contributions

A. Panneerselvam: conceptualization, validation, visualization, and writing – original draft. **R. Senthil Kumar:** validation and visualization. **V. M. Senthilkumar:** validation and visualization. **Kallapalli Anjani Devi:** validation and visualization. **S. Selvakumar:** conceptualization, investigation, writing – original draft, validation, visualization, formal analysis, and data curation. **S. C. Vella Durai:** conceptualization, investigation, funding acquisition, writing – original draft, writing – review and editing, visualization, validation, methodology, formal analysis, and resources.

Funding

This research did not receive specific funding from any public, commercial, or not-for-profit organizations.

Conflicts of Interest

The authors declare no conflicts of interest.

Data Availability Statement

No data was used in this study.

References

1. F. Zheng, M. Kotobuki, S. Song, M. O. Lai, and L. Lu, "Review on Solid Electrolytes for All-Solid-State Lithium-Ion Batteries," *Journal of Power Sources* 389 (2018): 198–213, https://doi.org/10.1016/j.jpowsour.2018.04.022.

2. J. C. Bachman, S. Muy, A. Grimaud, et al., "Inorganic Solid-State Electrolytes for Lithium Batteries: Mechanisms and Properties Governing Ion Conduction," *Chemical Reviews* 116 (2016): 140–162, https://doi.org/10.1021/acs.chemrev.5b00563.

3. J. Xiao, J. Wang, L. Fan, J. Zhang, and X. Li, "Recent Advances in $Li_{1+x}Al_xTi_{2-x}(PO_4)_3$ Solid-State Electrolyte for Safe Lithium Batteries," *Energy Storage Materials* 19 (2019): 379–400, https://doi.org/10.1016/j.ensm.2018.10.012.

4. F. Sudreau, D. Petit, and J. P. Boilot, "Dimorphism, Phase Transitions, and Transport Properties in $LiZr_2(PO_4)_3$," *Journal of Solid State Chemistry* 90 (1989): 78–90, https://doi.org/10.1016/0022-4596(89)90056-X.

5. C. Cao, Z. Bin Li, X. L. Wang, X. B. Zhao, and W. Q. Han, "Recent Advances in Inorganic Solid Electrolytes for Lithium Batteries," *Frontiers in Energy Research* 2 (2014): 25, https://doi.org/10.3389/fenrg.2014.00025.

6. C. A. Augustine, D. Panoth, and A. Paravannoor, "High Performance Li-Ion Battery Anodes Based on Si Nano Core in an LATP Matrix With Better Electrolyte Compatibility and Temperature Resistance," *ChemistrySelect* 4 (2019): 7090–7095, https://doi.org/10.1002/slct.201901208.

7. J. Fu, "Superionic Conductivity of Glass-Ceramics in the System Li_2O-Al_2O_3-TiO_2-P_2O_5," *Solid State Ionics* 96 (1997): 195–200, https://doi.org/10.1016/S0167-2738(97)00018-0.

8. A. Jetybayeva, B. Uzakbaiuly, A. Mukanova, S. T. Myung, and Z. Bakenov, "Recent Advancements in Solid Electrolytes Integrated Into All-Solid-State 2D and 3D Lithium-Ion Microbatteries," *Journal of Materials Chemistry A* 9 (2021): 15140–15178, https://doi.org/10.1039/D1TA02652F.

9. X. M. Wu, X. H. Li, Y. H. Zhang, M. F. Xu, and Z. Q. He, "Synthesis of $Li_{1.3}Al_{0.3}Ti_{1.7}(PO_4)_3$ by Sol–Gel Technique," *Materials Letters* 58 (2004): 1227–1230, https://doi.org/10.1016/j.matlet.2003.09.013.

10. M. Monchak, T. Hupfer, A. Senyshyn, et al., "Lithium Diffusion Pathway in $Li_{1.3}Al_{0.3}Ti_{1.7}(PO_4)_3$ (LATP) Superionic Conductor," *Inorganic Chemistry* 55 (2016): 2941–2945, https://doi.org/10.1021/acs.inorgchem.5b02821.

11. Q. Ma, Q. Xu, C. L. Tsai, F. Tietz, and O. Guillon, "A Novel Sol–Gel Method for Large-Scale Production of Nanopowders: Preparation of $Li_{1.5}Al_{0.5}Ti_{1.5}(PO_4)_3$ as an Example," *Journal of the American Ceramic Society* 99 (2016): 410–414, https://doi.org/10.1111/jace.13997.

12. S. Duluard, A. Paillassa, L. Puech, et al., "Lithium Conducting Solid Electrolyte $Li_{1.3}Al_{0.3}Ti_{1.7}(PO_4)_3$ Obtained via Solution Chemistry," *Journal of the European Ceramic Society* 33 (2013): 1145–1153, https://doi.org/10.1016/j.jeurceramsoc.2012.08.005.

13. K. Kwatek and J. L. Nowi, "Electrical Properties of $LiTi_2(PO_4)_3$ and $Li_{1.3}Al_{0.3}Ti_{1.7}(PO_4)_3$ Solid Electrolytes Containing Ionic Liquid," *Solid State Ionics* 302 (2016): 54–60, https://doi.org/10.1016/j.ssi.2016.11.020.

14. N. Anantharamulu, K. Koteswara Rao, G. Rambabu, B. Vijaya Kumar, V. Radha, and M. Vithal, "A Wide-Ranging Review on Nasicon Type Materials," *Journal of Materials Science* 46 (2011): 2837, https://doi.org/10.1007/s10853-011-5302-5.

15. K. G. Schell, E. C. Bucharsky, F. Lemke, and M. J. Hoffmann, "Effect of Calcination Conditions on Lithium Conductivity in $Li_{1.3}Ti_{1.7}Al_{0.3}(PO_4)_3$ Prepared by Sol-Gel Route," *Ionics* 23 (2017): 821–827, https://doi.org/10.1007/s11581-016-1883-y.

16. M. A. Subramanian, R. Subramanian, and A. Clearfield, "Lithium Ion Conductors in the System $AB(IV)_2(PO_4)_3$ (B = Ti, Zr and Hf)," *Solid State Ionics* 18–19 (1986): 562–569, https://doi.org/10.1016/0167-2738(86)90179-7.

17. Q. Liu, H. Lin, J. Zhao, et al., "Garnet and $Li_{29}Zr_9Nb_3O_{40}$ Modified PEO-Based Hybrid Solid Electrolytes for All-Solid-State Lithium Metal Batteries," *European Journal of Inorganic Chemistry* 27 (2024): e202400137, https://doi.org/10.1002/ejic.202400137.

18. A. G. Jolley, G. Cohn, G. T. Hitz, and E. D. Wachsman, "Improving the Ionic Conductivity of NASICON Through Aliovalent Cation Substitution of $Na_3Zr_2Si_2PO_{12}$," *Ionics* 21 (2015): 3031–3038, https://doi.org/10.1007/s11581-015-1498-8.

19. X. Yang, D. Kong, Z. Chen, Y. Sun, and Y. Liu, "Low-Temperature Fabrication for Transparency Mg Doping $Li_7La_3Zr_2O_{12}$ Solid State Electrolyte," *Journal of Materials Science: Materials in Electronics* 29 (2018): 1523–1529, https://doi.org/10.1007/s10854-017-8062-4.

20. W. Yang, B. Wang, Q. Chen, et al., "Unravelling Capacity Fading Mechanisms in Sodium Vanadyl Phosphate for Aqueous Sodium-Ion Batteries," *Journal of Colloid and Interface Science* 627 (2022): 913–921, https://doi.org/10.1016/j.jcis.2022.07.108.

21. S. Zhang, H. Zhao, J. Guo, Z. Du, J. Wang, and K. Swierczek, "Characterization of Sr-Doped Lithium Lanthanum Titanate With Improved Transport Properties," *Solid State Ionics* 336 (2019): 39–46, https://doi.org/10.1016/j.ssi.2019.03.015.

22. S. Kumar and P. Balaya, "Improved Ionic Conductivity in NASICON-Type Sr^{2+} Doped $LiZr_2(PO_4)_3$," *Solid State Ionics* 296 (2016): 1–6, https://doi.org/10.1016/j.ssi.2016.08.012.

23. C. M. Julien, A. Mauger, K. Zaghib, R. Veillette, and H. Groult, "Structural and Electronic Properties of the $LiNiPO_4$ Orthophosphate," *Ionics* 18 (2012): 625–633, https://doi.org/10.1007/s11581-012-0671-6.

24. S. Stegmaier, K. Reuter, and C. Scheurer, "Exploiting Nanoscale Complexion in LATP Solid-State Electrolyte via Interfacial Mg^{2+} Doping," *Nanomaterials* 12 (2022): 2912, https://doi.org/10.3390/nano12172912.

25. S. Selvakumar, S. G. Pushpalatha Gracelin, S. C. Vella Durai, R. Venkatesh, and S. Sudharthini, "Preparation, Microstructure and Conductivity Study of $Li_{1.3}Al_{0.3}Ti_{1.7}(PO_4)_3$ Solid Electrolytes for Lithium Ion Batteries," *Physics of the Solid State* 67 (2025): 1010–1018, https://doi.org/10.1134/S1063783425602413.